Materialia 14 (2020) 100934

Contents lists available at ScienceDirect

Materialia

journal homepage: www.elsevier.com/locate/mtla

Full Length Article

Development of computational framework for titanium alloy phase transformation prediction in laser powder-bed fusion additive manufacturing

Zhi Liang[a,*], Ivan Zhirnov[b], Fan Zhang[c], Kevontrez K. Jones[d], David Deisenroth[b], Maureen Williams[a], Ursula Kattner[a], Kil-won Moon[a], Wing-Kam Liu[d], Brandon Lane[e], Carelyn Campbell[a]

[a] Materials Science and Engineering Division, Material Measurement Laboratory, National Institute of Standards and Technology, 100 Bureau Drive, Gaithersburg, MD 20899, United States
[b] Sensor Science Division, Physical Measurement Laboratory, National Institute of Standards and Technology, 100 Bureau Drive, Gaithersburg, MD 20899, United States
[c] Materials Measurement Science Division, Material Measurement Laboratory, National Institute of Standards and Technology, 100 Bureau Drive, Gaithersburg, MD 20899, United States
[d] Department of Mechanical Engineering, Northwestern University, Evanston, IL 60208-3109, United States
[e] Intelligent Systems Division, Engineering Laboratory, National Institute of Standards and Technology, 100 Bureau Drive, Gaithersburg, MD 20899, United States

ARTICLE INFO

Keywords:
CALPHAD
Computational fluid dynamics
Additive manufacturing
Titanium alloys
Phase transformation prediction

ABSTRACT

In conjunction with bare metal single laser track validation experiments, a computational framework is proposed to accelerate the design and development of new additive manufacturing (AM) specific alloys. Specifically, Additive Manufacturing-Computational Fluid Dynamics (AM-CFD) and Calculation of Phase Diagram (CALPHAD), were combined to predict location-specific $\beta \rightarrow \alpha$ phase transformation for a new Ti-Al-Fe-alloy. This modeling work was validated by rigorous spatially resolved synchrotron-based X-ray diffraction measurements. This framework reasonably predicts the melt pool and heat affected zone features in the experiment and reveals their significance in actual AM conditions. This framework can be applied for rapid and comprehensive evaluation of location-specific thermal history, phase, microstructure, and properties for new AM titanium alloy development.

1. Introduction

Titanium (Ti) alloys have attracted interest as structural materials due to their outstanding balance between various properties, such as high tensile strength and toughness, and low density [1]. Currently the commercial Ti alloy market is still mainly dominated by Ti-6Al-4 V alloy (Ti-64,%, mass fraction), developed in 1954 as a forging alloy. In addition to classical airframe and aero-engine structural applications, Ti alloys can be tailored to meet performance requirements for a variety of applications, such as biomedical implants with low elastic moduli, corrosion resistant alloys for the chemical and power industries, and low-cost, high-strength-to-weight-ratio alloys for automotive components.

The majority of commercial Ti alloys are still manufactured using conventional wrought processing technology that employs casting ingots followed by various thermo-mechanical processes [2]. Additive manufacturing (AM) processing is often preferable for lowering the cost for titanium alloy component fabrication as AM can produce near net-shape components with complex geometry and avoids costly metal-removal steps required in most conventional processes. This advantage has spurred significant research efforts into optimizing AM processes for the Ti-6Al-4 V alloy. Liu et al. [3] concluded that the higher cooling rates associated with laser bed power fusion (LPBF) and direct energy deposition (DED) processing, compared with conventional process such as casting, led to the formation of acicular α' martensitic microstructure and high tensile stresses. On the contrary, with similar slower cooling rates but higher build temperatures, electron beam melting (EBM) produced α lamellar microstructure with little residual stresses. Although the EBM produced Ti microstructures are preferred, the LPBF and DED processes allow for more complex build geometries [3,4]. Thus, the design of AM Ti alloys that are tailored to the LPBF and DED process would enable wider adoption of the AM Ti parts.

Ti alloy design relies on controlling the allotropic transformation from the high temperature body-centered cubic (BCC) β phase to the low temperature hexagonal close packed (HCP) α phase, which is essential to Ti alloy properties. The fraction of retained β phase can be controlled by the amount of β-stabilizing elements such V, Mo, Fe, and

* Corresponding author.
E-mail addresses: zhi.liang@nist.gov, liang.460@osu.edu (Z. Liang).

https://doi.org/10.1016/j.mtla.2020.100934
Received 4 August 2020; Accepted 11 October 2020
Available online 16 October 2020

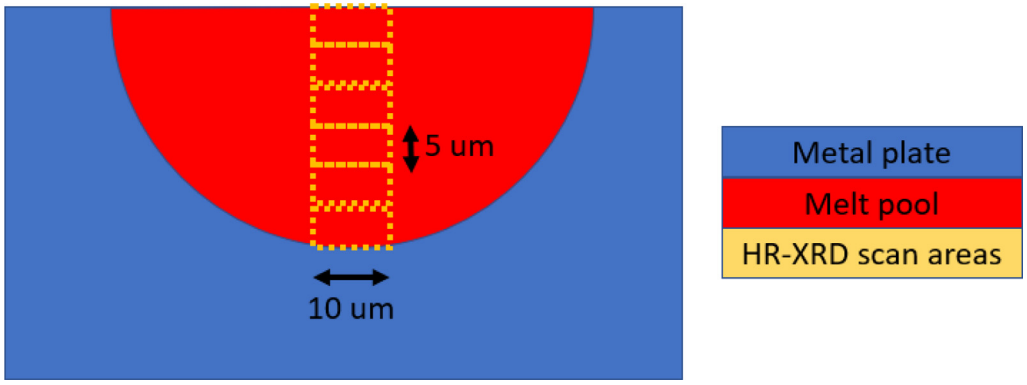

Fig. 1. Schematic of HR-XRD measurement. Each dashed yellow box represents one measurement step.

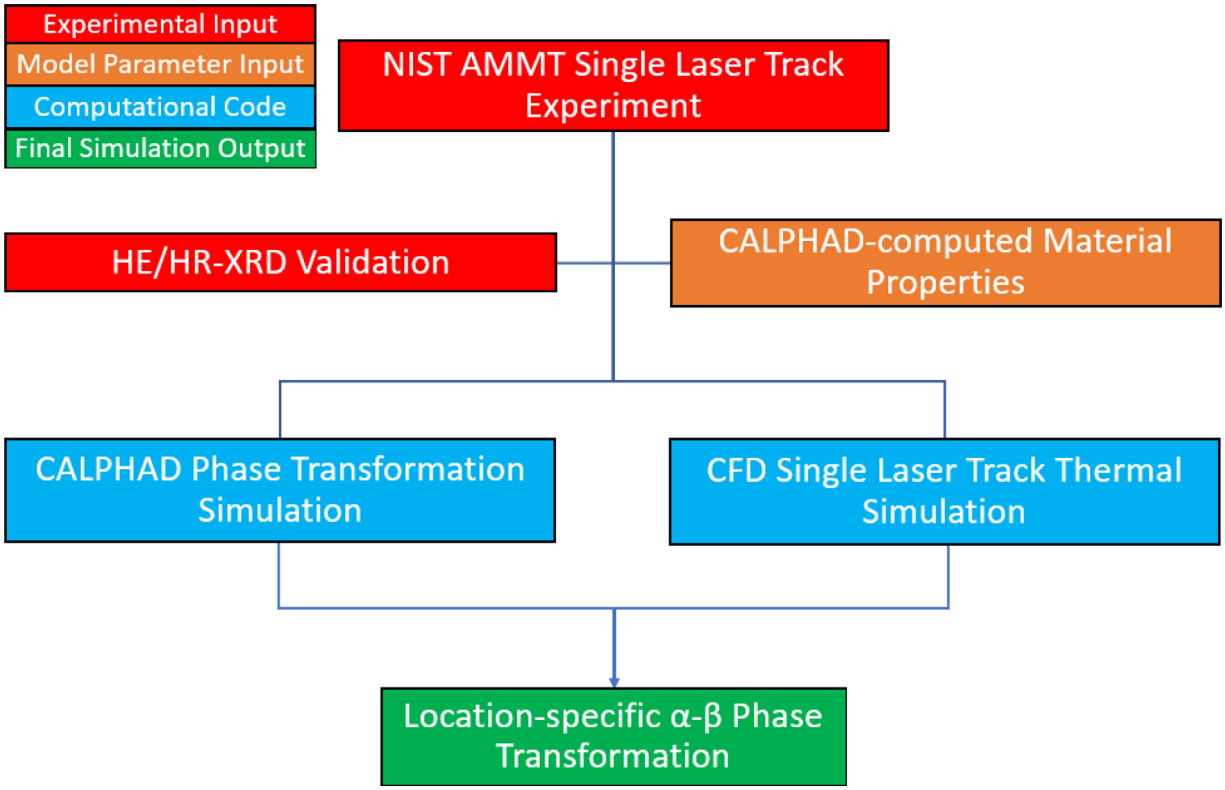

Fig. 2. Experimental and modeling works flowchart.

Mn. Both V and Mo are isomorphous β stabilizers and do not form intermetallics with Ti. In contrast, Fe and Mn are both eutectoid β stabilizers and readily form intermetallics with Ti. However, the desire to produce lower-cost, high-strength, and low-density Ti alloys, particularly for automotive applications, make Fe an attractive replacement for V.

In addition, eutectoid β stabilizers, compared with isomorphous β stabilizers, have another major disadvantage in conventional titanium manufacturing processes As these elements are rejected from the freezing interface resulting in either micro-scale or macro-scale segregation depending on local thermal gradient, in which the macro-segregation forms "β fleck" or localized inhomogeneous β-stabilizer-rich regions with lower β transus [1,5,6]. On the contrary, in AM processes, the localized rapid solidification restricts the partitioning of alloying elements, and therefore enables eutectoid β stabilizers to be reconsidered in AM titanium alloy design [7]. Using a Calculation of Phase Diagram (CALPHAD)-based design approach, Liang et al. [8] designed a potential low-cost Ti-Al-Fe based alloy that appeared promising and avoids the formation of the TiFe intermetallics. Based on the initial casting results, this alloy may also be potential candidate for AM LPBF and DED processes.

To evaluate new potential AM Ti alloys, this work conducted a single laser trace experiments, which are known to be governed by the same physics as LPBF [9], to evaluate this alloy and correlate the observed microstructure with the LPBF processing parameters. This experiment applies a laser with a designated set of parameters on a bare alloy substrate to characterize the melt pool and the interaction between melt pool and alloy base plate. Although there are discrepancies between single laser trace experiment and actual build, this method offers a fast evaluation of performances of new potential alloys in LBPF before proceeding to customized powder fabrication prototyping, which significantly accelerates AM alloy development. Based on these experiments and result characterizations, a framework to predict the location-specific $\beta \rightarrow \alpha$ phase transformation was developed using computational fluid dynamics (CFD) and CALPHAD methods. CFD was used to determine the temperature profiles as function of locations, and using these temper-

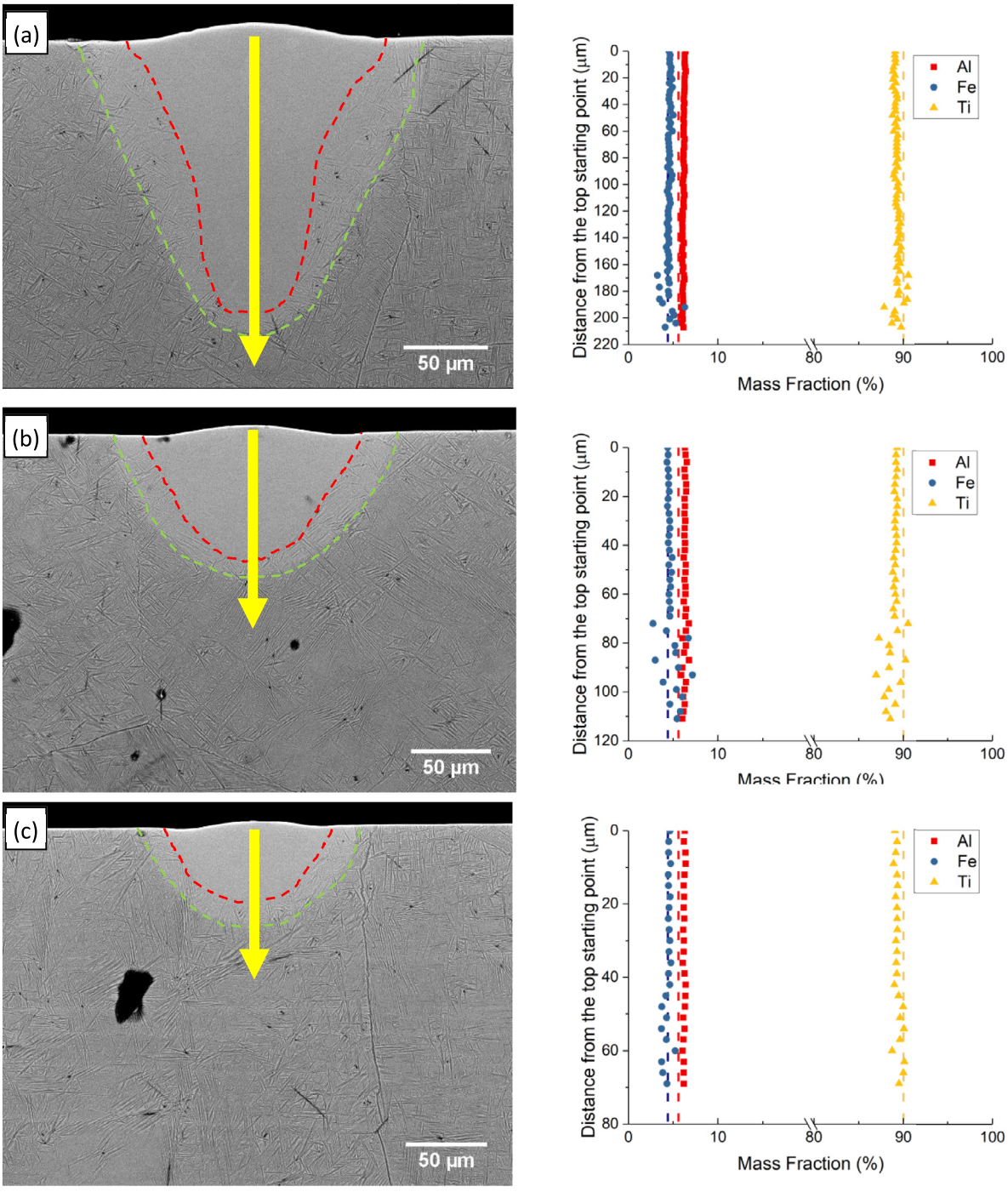

Fig. 3. Backscattered cross-sectional images of single laser track at different laser speeds and corresponding EDXS line scan profiles: (a) 400 mm/s, (b) 700 mm/s, (c) 1000 mm/s. Melt pool boundaries (red-dashed), heat affected zone (green-dashed) boundaries, and EDXS line scan directions (solid-yellow) are shown. The dashed lines in EDXS line scan represent the bulk spectrum analysis of the bare plate matrix. The dashed lines in SEM images are for eye-guidance purpose only. (For interpretation of the references to colour in this figure legend, the reader is referred to the web version of this article.)

ature profiles as input, the CALPHAD method was used to predict the phase transformation behavior.

2. Materials, experimental methods, and computational tools

2.1. Materials preparation

Nominal composition of the prototype alloy is Ti-6Al-5Fe-0.05B-0.05C (%, mass fraction), as reported by Liang et al. [8]. The raw materials are high purity titanium (99.995%, Advanced Material Professional Manufacture[1]), aluminum (99.9999%, Cominco American, iron (99.98%, Alfa Aesar), boron (99.999%, Alfa Aesar) and carbon (99%,

[1] Certain commercial equipment, instruments, or materials are identified in this paper to foster understanding. Such identification does not imply recommendation or endorsement by the National Institute of Standards and Technology, nor does it imply that the materials or equipment identified are necessarily the best available for the purpose. The opinions, recommendations, findings, and conclusions in this publication do not necessarily reflect the views or policies of NIST or the United States Government.

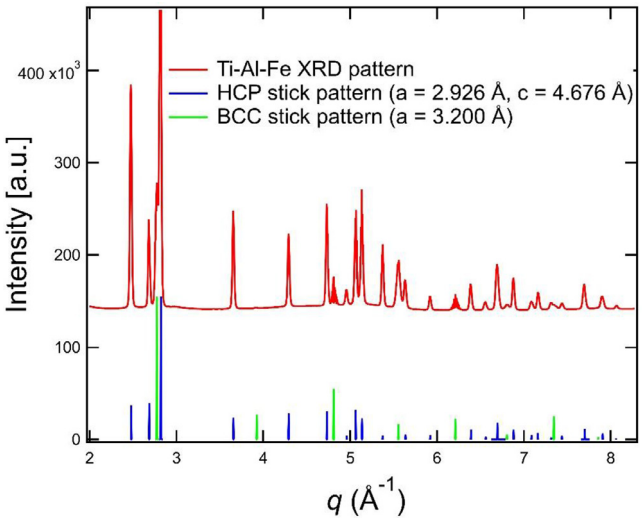

Fig. 4. XRD pattern of the as-cast bare plate matrix.

Alfa Aesar). A 30-gram alloy was casted using an arc melter. Before melting, the chamber was evacuated and then maintained a 67.7 kPa (50.8 mmHg) partial Ar pressure during melting to minimize contamination from the air. As part of the casting process, the button was flipped and re-melted 5 times to ensure homogeneity. For the prepared specimen, the compositions of major alloying elements (Ti, Al, Fe) were analyzed by scanning electron microscope energy dispersive X-ray spectrometry (SEM-EDXS), and the oxygen content was analyzed by Luvak Inc. following ASTM standard E1409–13. The nominal and measured compositions are listed in Table 1.

Table 1
Nominal and measured compositions of sample alloy.

Composition (%, mass fraction)	Ti	Al	Fe	B	C	O
Nominal	Bal.	6	5	0.05	0.05	N/A
Measurement	Bal.	5.59	4.41	N/A	N/A	0.038

2.2. Experimental methods

2.2.1. Single laser track experiment

The sample button was sliced into thin plates that were 2 mm × 12 mm × 10 mm (thickness × length × width) in size. These plates were polished to 800-grit surface for the single laser track experiment. The single laser track experiment was performed on National Institute of Standards and Technology Additive Manufacturing Metrology Testbed (NIST-AMMT) system [10], which incorporates a high-speed, high-magnification staring image system (static field of view position directly in working zone) and a wide range of metrological tools to investigate melt pool temperature and dynamic phenomena. The process-

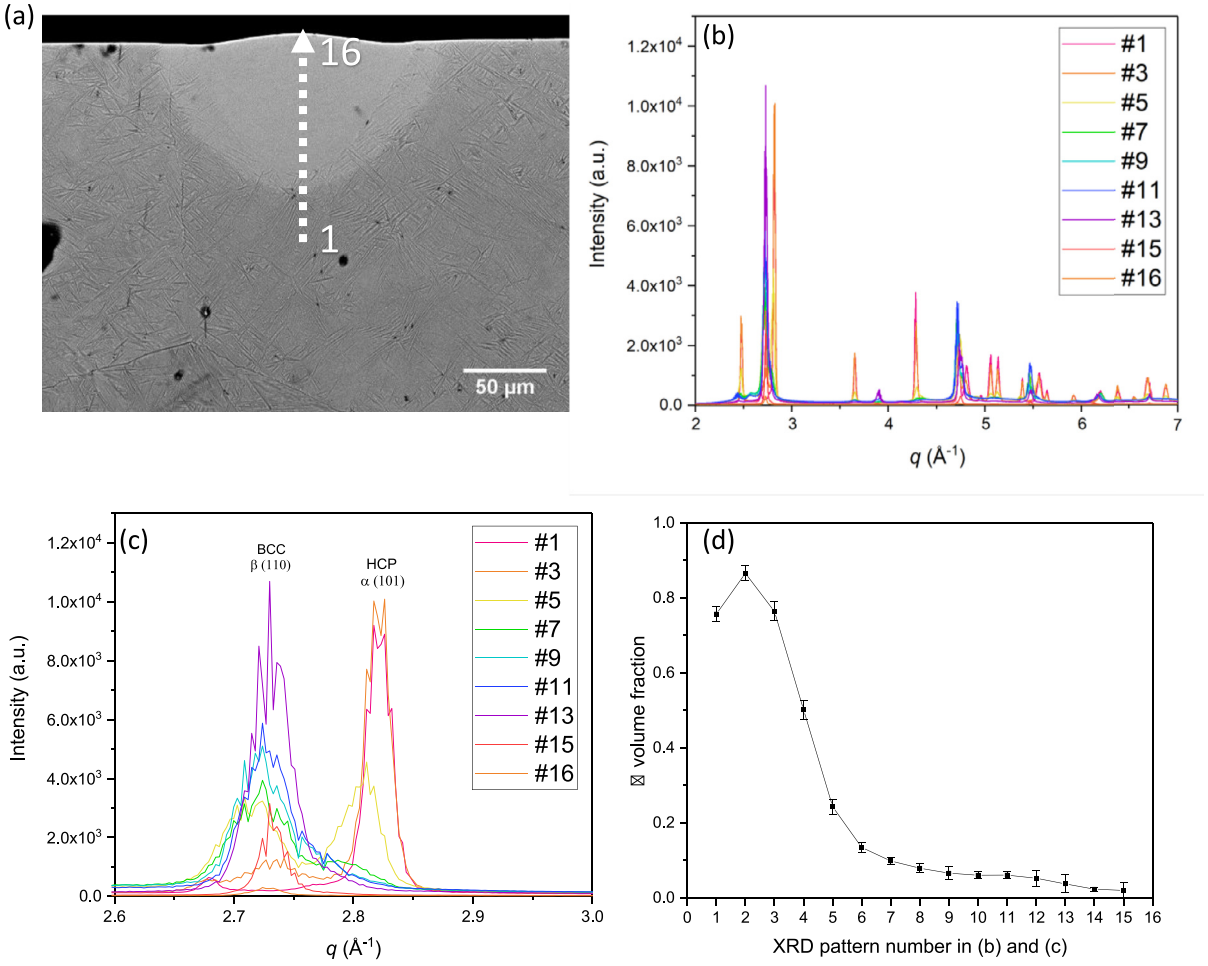

Fig. 5. (a) 700 mm/s cross-section SEM back-scattered electron image, arrow and numbers correspond to the numbers in (b and c) location-specific XRD patterns (overall and zoom-in). XRD patterns #1 to #15 were converted to α phase fraction and plotted in (d). Note: XRD pattern #15 had low peak intensity and the α phase fraction could not be reliably calculated. Therefore, its phase fraction value was assumed as 0.02 and was given a 0.02 error bar.

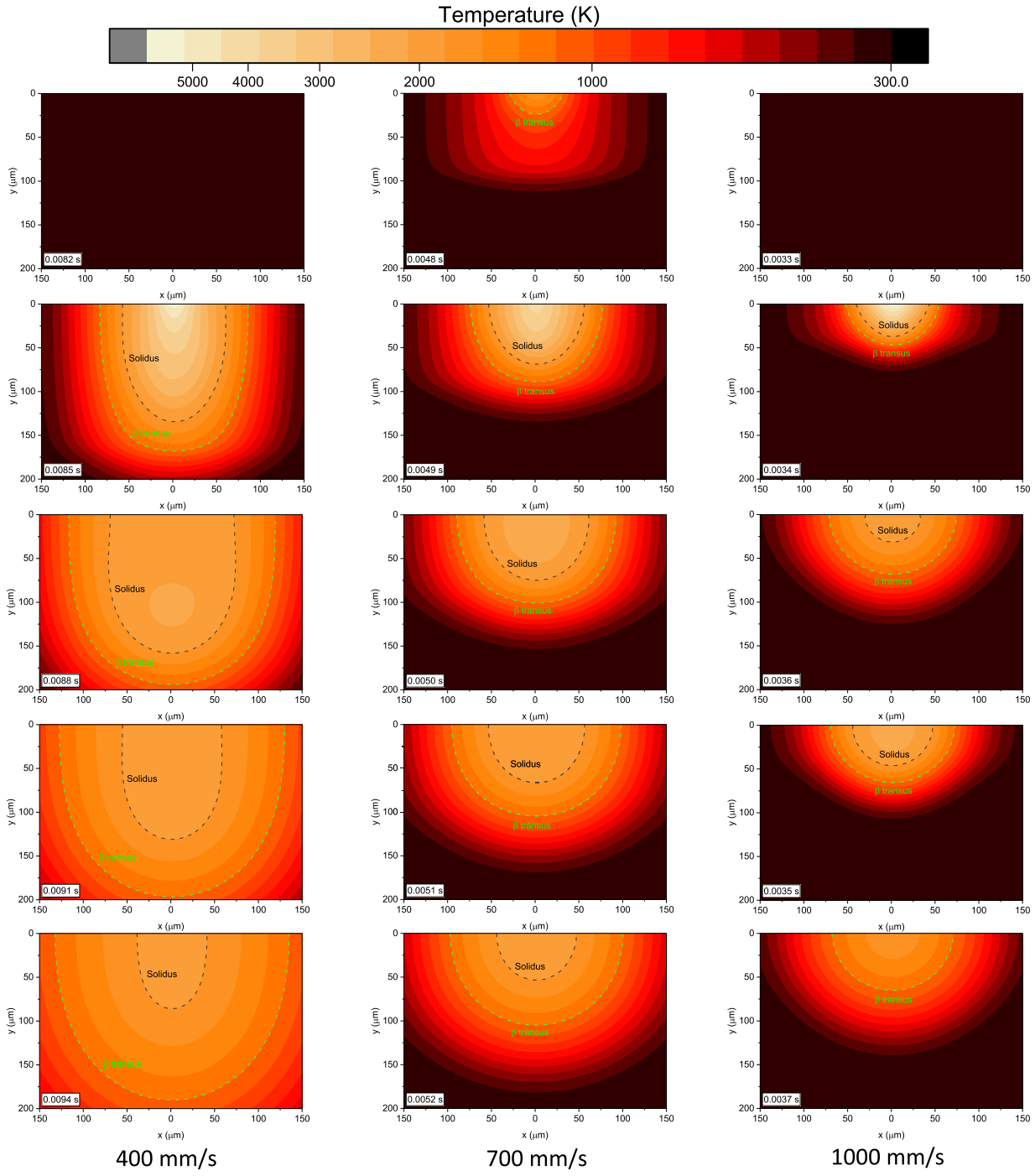

Fig. 6. Simulated temperature evolutions of cross-sectional areas at different laser speeds and time steps: (left to right) 400 mm/s, 700 mm/s, 1000 mm/s. Black-dashed and green-dashed lines are solidus and β transus contours respectively.

ing chamber has inert gas (Ar) flow environment to avoid oxidation. The laser scan was conducted with a laser power of 100 W and spot size of 30 μm at 3 different laser speeds: 400 mm/s, 700 mm/s, and 1000 mm/s. The track length was 6 mm and the distance between neighboring tracks was 1 mm. Each laser speed was repeated 3 times and the track with the smoothest surface condition was selected for further characterization.

2.2.2. Scanning electron microscopy (SEM) and energy dispersive X-ray spectroscopy (EDXS)

The single laser track specimens were cross-sectioned at the mid-point of the track length in the laser-stable smooth region. The cross-sections were characterized by SEM, and the composition of the alloy (for major alloying elements) was measured using SEM-EDXS with the standard Perkin-Elmer 2D area detector and at an operating voltage of 20 kV, which is reported in Table 1.

2.2.3. High energy X-ray diffraction (HE-XRD)

Synchrotron-based high-energy X-ray diffraction (HE-XRD) experiments were performed to determine the α and β phase fractions of the base alloy plate as the starting condition in CALPHAD phase transformation simulation.

The HE-XRD measurements were performed in the transmission mode at beamline 11-ID-B of the Advanced Photon Source, Argonne National Laboratory. The X-ray wavelength is 0.021130 nm (0.21130 Å),

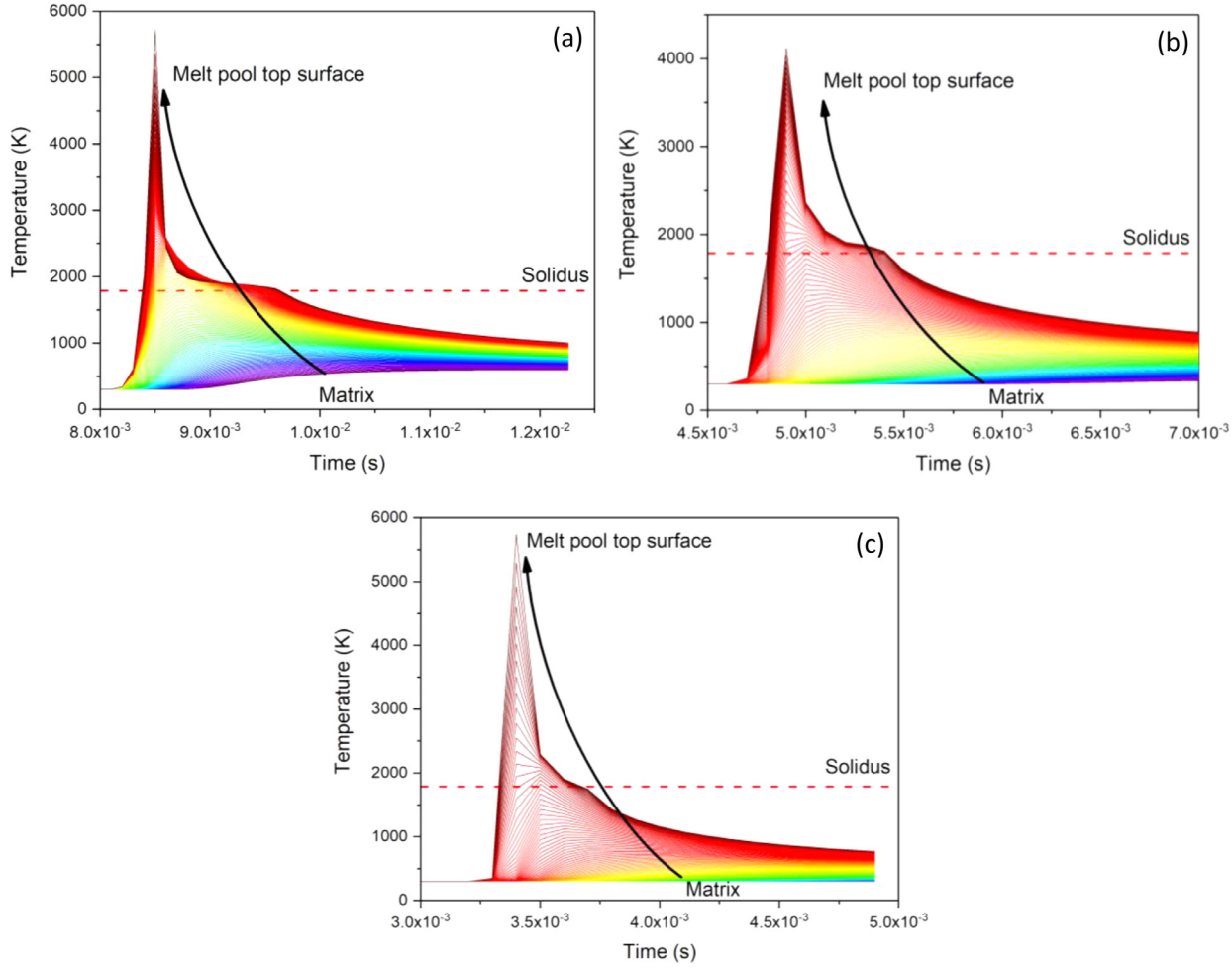

Fig. 7. Simulated temperature profiles of cross-sectional area centerlines of single laser track at different laser speeds: (a) 400 mm/s, (b) 700 mm/s, (c) 1000 mm/s. The profiles from bottom to top are from matrix to melt pool top surface, marked by the black arrow.

which corresponds to an X-ray energy of 58.68 keV. The X-ray flux density is on the order of 10^{13} photon•mm^{-2}•s^{-1}. With the standard Perkins-Almer 2D area detector at the beamline and a sample to detector distance of 750 mm, this setup allows a continuous q range of 2.5 nm^{-1} (0.25 Å^{-1}) to 77.5 nm^{-1} (7.75 Å^{-1}), where $q = 2\pi/\lambda \times \sin(\theta)$, with θ being one half of the diffraction angle 2θ and λ being the X-ray wavelength. The sample was ≈ 1 mm in thickness. X-ray beam size was 300 μm × 300 μm. 10 XRD measurements were acquired with an acquisition time of 1 s each. The reported data are the sum of 10 XRD measurements.

2.2.4. High-Resolution X-ray diffraction (HR-XRD)

Due to the fine scale of the α precipitates in the microstructure of Ti-Al-Fe, it was difficult to reliably quantify the phase fractions with SEM resolution or the in-house X-ray diffraction measurements. SEM does not have the required spatial resolution to characterize the spatially-resolved phase fraction of the melt pool, and the in-house X-ray diffraction lacks sufficient penetration depths (Cu Kα radiation can only penetrate ≈ 5 μm of Ti alloy in the Bragg-Brentano geometry). To overcome these limitations, synchrotron-based high-resolution X-ray diffraction (HR-XRD) experiments were performed, again in transmission mode, to measure the bulk, location-specific phase fractions along the cross-section of laser track to validate CALPHAD model predictions.

To facilitate this measurement, a slice of the sample was cut perpendicular to the laser scan direction with a thickness of ≈ 1 mm in the middle of the track, where it can reasonably be assumed that the thermal history and melt pool microstructure are uniform across the 1 mm sample thickness. The same HE-XRD instrument at 11-ID-B of the Advanced Photon Source was used in this experiment at the same energy and with the same detector. The main difference is that the X-ray beam was reduced to a spot size of 10 μm (horizontal) × 5 μm (vertical) using a series of compact refractive lenses along the vertical direction and slitting along the horizontal direction as shown in the schematic in Fig. 1.

Spatial-resolved XRD experiments were performed along the vertical direction across the centerline of the 700 mm/s melt pool for calibration, with neighboring measurement positions 5 μm apart. At each sample position, 3 XRD patterns were acquired with an acquisition time of 3 s each. The reported data are based on the sum of 3 XRD patterns at each sample position.

In both HE-XRD and HR-XRD, the XRD peak intensity analysis is used to estimate the volume fractions of α and β phases. The detailed methodology was illustrated in another publication and not repeated here [11].

2.3. Computational tools

For each specific location in the bare metal plate, the phase transformation is dependent on the location-specific temperature profiles. There are two computational tools used in this work: CFD [12] for determination of location-specific temperature profiles, and CALPHAD method for determination of location-specific phase transformation with the temperature profiles predicted by CFD. The CALPHAD database also enables phase/composition-based material properties to be calculated and

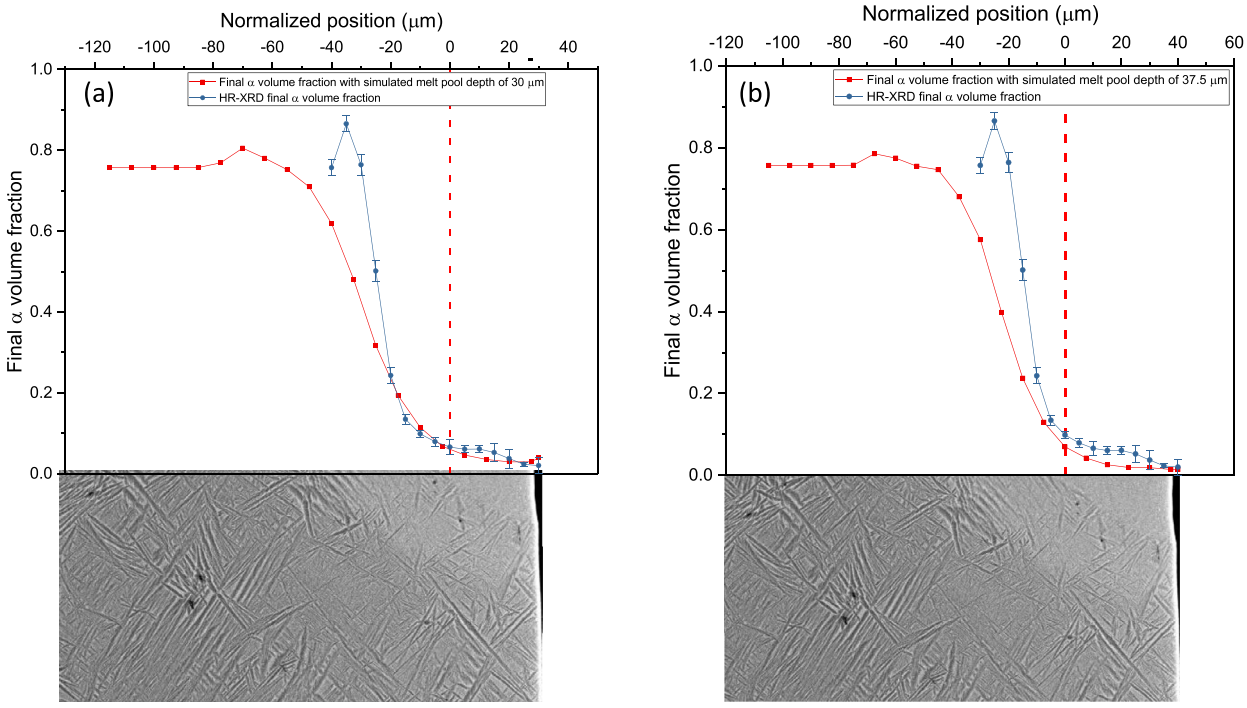

Fig. 8. Simulated (red) and HR-XRD measured (blue) α phase fractions in 700 mm/s case, compared with experimental cross-section, in which the black and red dashed-lines are metallurgically-observed melt pool and heat affected zone boundaries respectively. The simulated profiles were at melt pool depths of (a) 30 μm and (b) 37.5 μm respectively. Error bars in experimental data represent the uncertainties of HR-XRD measurements, except for the 0.02 error bar for the right-most location as illustrated in Fig. 5. (For interpretation of the references to colour in this figure legend, the reader is referred to the web version of this article.)

applied in these two computational tools. The input-output relationship between experiments and models is illustrated in Fig. 2.

2.3.1. Additive manufacturing-computational fluid dynamics (AM-CFD)

The single laser track experimental setup information and computed material parameters are used as input into the CFD simulation to determine the location-specific temperature profiles for the entire specimen [12], especially for the region below specimen surface, which is usually difficult or impossible to be directly measured.

2.3.2. of phase diagram (CALPHAD)

2.3.2.1. Databases. To convert the location-dependent cooling profile from CFD to phase transformation profile, a precipitation/dissolution simulation was conducted. An essential requirement for these simulations is thermodynamic and kinetic descriptions of the target alloy system. For this work, authors have developed a customized Ti-Al-Fe thermodynamic and kinetic [13–18] descriptions. The development of these descriptions will be described in a separate paper. As B and C are not major alloying elements but act as grain refiner, forming TiB and TiC, these elements are not included in the descriptions for simplicity. In this simulation, two phases from the description are used: β (BCC_A2, (Al, Fe, Ti)$_1$(Va)$_3$) and α (HCP_A3, (Al, Fe, Ti)$_1$(Va)$_{0.5}$). The description is included in the Supplementary Information.

2.3.2.2. TC-PRISMA precipitation simulation. The TC-PRISMA software [12] was used to predict the location/time-specific precipitate (α) volume fraction evolutions as a function of the temperature profiles generated by the CFD simulations. TC-PRISMA is based on Kampmann-Wagner numerical (KWN) model [19] to simulate the nucleation, growth, coarsening, and dissolution of precipitates. This method predicts the phase transformation using inputs from the multicomponent thermodynamics/kinetics databases, user-defined temperature profiles, and initial alloy compositions/phase fractions. Based on these inputs, TC-PRISMA can estimate precipitate size distribution, its corresponding number density, mean radius and volume fraction. In this work, the simulations are focused on predicting location-specific α phase volume fraction profiles as functions of the simulated temperature profiles from CFD. The location-specific final α volume fractions are validated by HR-XRD measurements.

2.3.2.3. Nucleation and growth/homogenization models. In this work, the bulk-site nucleation and general growth models were used. In reality, the precipitate nucleation is more likely to occur heterogeneously on grain boundaries and dislocations. However, in the single laser track experiment, the laser spot size and melt pool size were smaller than β grain size, which excluded grain boundary nucleation in this experiment. As for dislocations, the dislocation-based heterogenous nucleation model requires the dislocation density as the input parameter, which is experimentally unavailable for the present work. Therefore, the bulk-site nucleation model was applied, assuming every atom in the pre-defined space as a potential nucleation site and avoiding dislocation density parameter assumption [20]. The general growth/homogenization model is based on Morral-Purdy model with cross-diffusion consideration [19]. These two models are described in detail in TC-PRISMA module [20]. All the parameters used in the model were calculated from the customized Ti-Al-Fe database except for the needle-shape precipitates for which the geometrical length-to-radius aspect ratio was assumed as 3 based on experimental microstructure in Fig. 3.

3. Results and discussion

3.1. Experimental results and discussion

3.1.1. Single laser track microstructure characterization

SEM backscattered images of laser track cross-sections in Fig. 3 show the microstructures of melt pool for all three laser scan speeds of 400 mm/s, 700 mm/s, and 1000 mm/s, respectively. The melt pool boundaries, heat affected zones, and unaffected bare plate matrix can be visually distinguished in all three cross-sections. The size of the melt

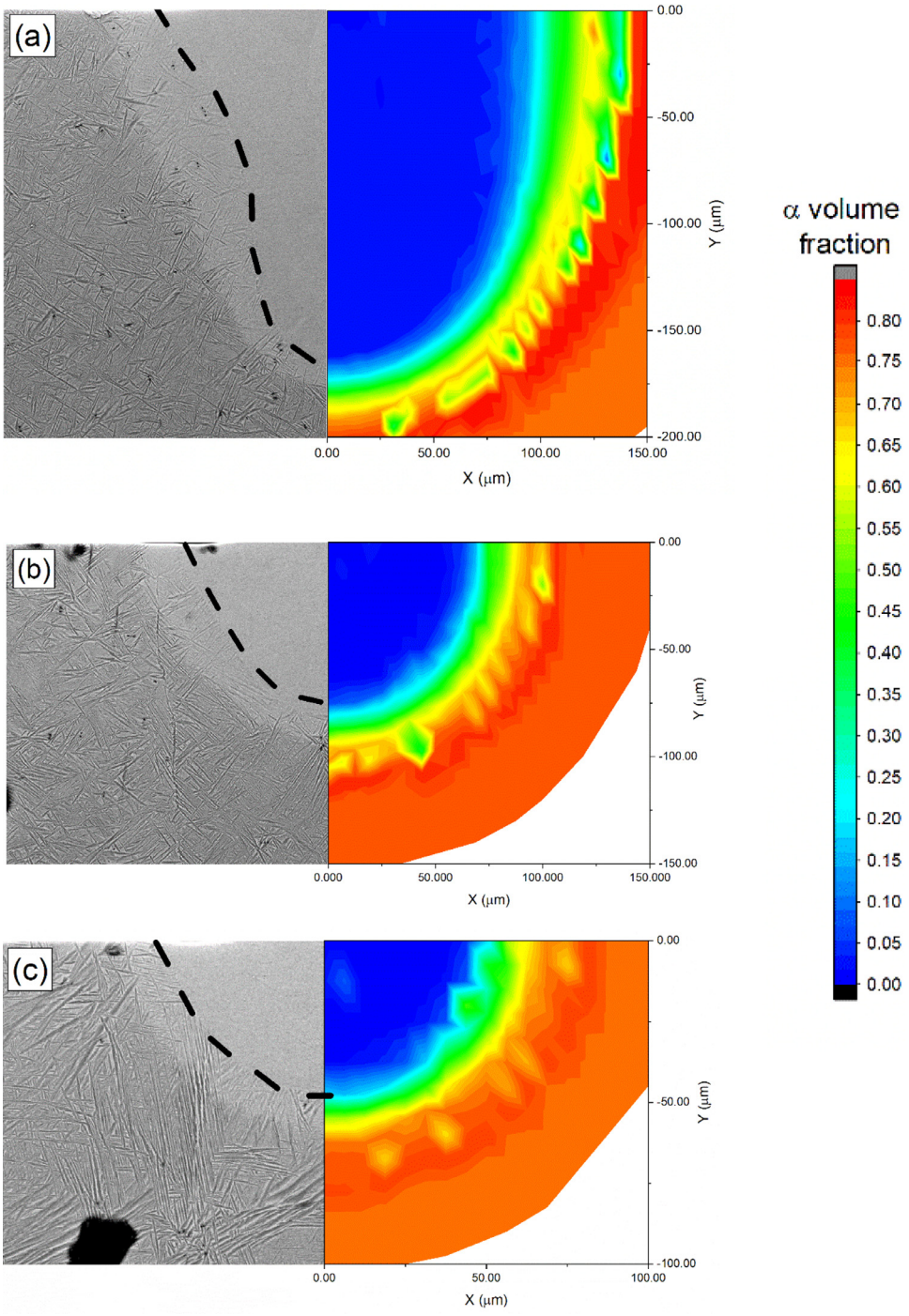

Fig. 9. CALPHAD-simulated location-specific α phase final volume fraction compared with microscopy cross-sections at different laser speeds: (a) 400 mm/s (b) 700 mm/s (c) 1000 mm/s. The black-dashed lines are metallurgically observed melt pool boundaries.

pool increased as the laser speed decreased because of the increasing heat input. It can also be observed that in the 400 mm/s case, the keyhole feature [21] was produced. EDXS composition line scans in Fig. 3 indicate that there were no significant discrepancies between the compositions measured within the melt pool and inside the bare plate matrix, indicating that no macro-segregation occurred. It should be noted that as the EDXS line scan went into the heat affected zone and the matrix, the elemental compositions start to fluctuate, which is due to the point analysis hitting both α and β phases, resulting in the fluctuation of compositions. Therefore, the bulk spectrum in the matrix is plotted in Fig. 3 as dashed lines representing the entire matrix composition.

A heat affected zone is defined as the region that retained precipitate morphologies consistent with the matrix and is adjacent to melt pool. This heat affected zone occurs as a result of the intensive heat from the melt pool and the low thermal conductivity associated with Ti alloys. The presence of the heat-affected zone for this Ti-Al-Fe alloy at all three laser speeds indicates that this alloy is susceptible to intensive heat from the laser. SEM observation of the heat-affected zones implies that the width of the zone is correlated to the laser speed and that as-fabricated microstructure and properties could potentially be tailored by laser input parameters directly. Due to the limitation of contrast differentiation and resolution of EDXS, the actual heat affected zone sizes could not be quantified without additional measurements.

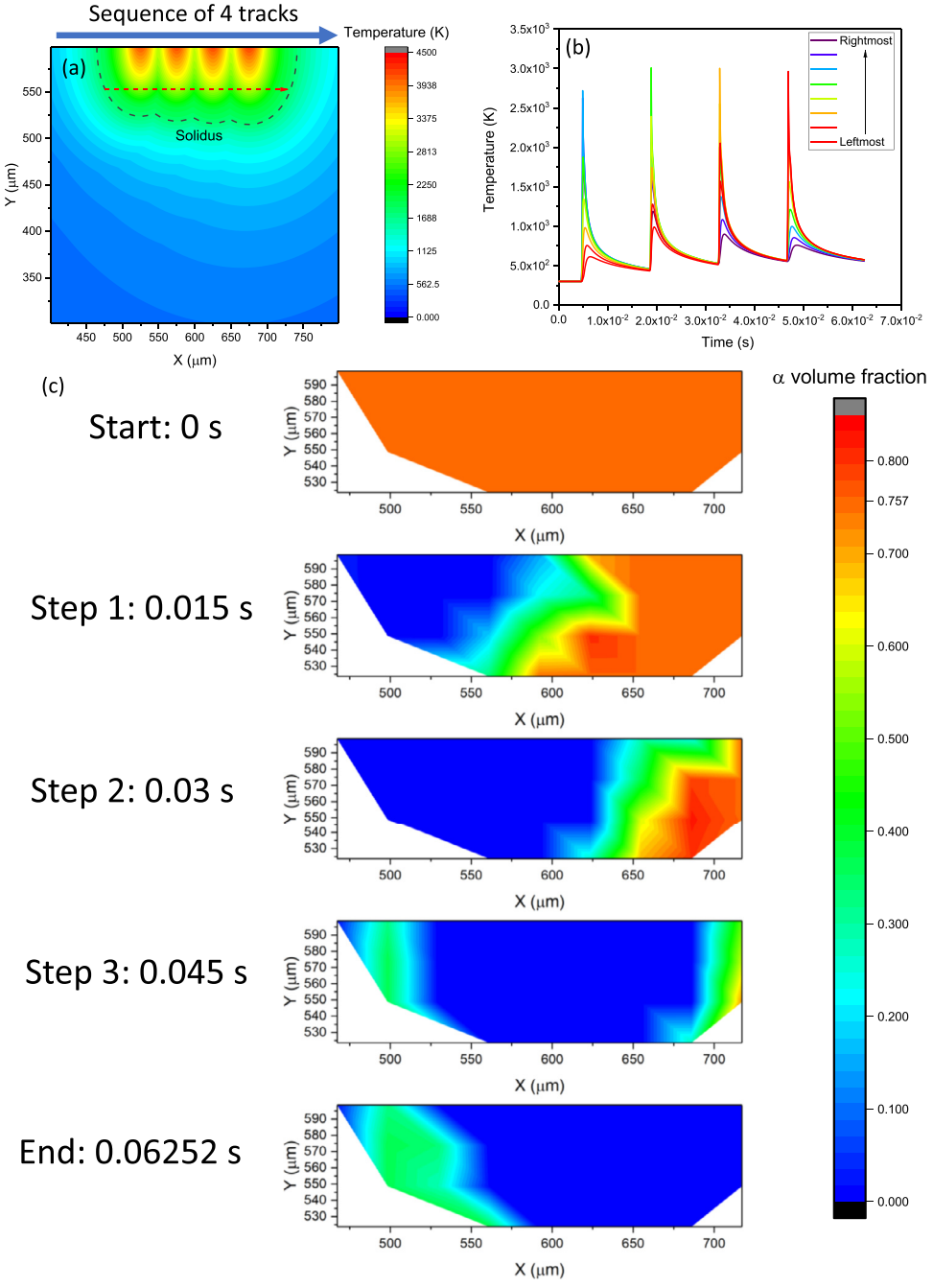

Fig. 10. (a) Simulated maximum temperature contour of cross-sectional areas in 4-track setup. (b) Several simulated temperature profiles along the sequence of tracks (red dashed line in (a)), in which the arrow indicates that the color of the tracks from leftmost to rightmost position. (c) α phase fraction evolution maps at different time step in the melt pool.

3.1.2. Phase quantification of the starting condition and laser track cross-section

The reduced HE-XRD pattern of the base alloy plate prior to laser scan is shown in Fig. 4. The starting matrix is fully described by a combination of α and β phases. The deduced volume fractions of α and β phases from the pattern were 75.7% and 24.3% respectively, with an uncertainty of ±0.7%. This experimental measurement was used to define the starting phase fraction in CALPHAD phase transformation simulation.

To better quantify the width of the heat affected zone, HR-XRD measurements were conducted. As shown in Fig. 5, 16 XRD patterns from the 700 mm/s melt pool centerline are plotted in the same figure to represent the phase fraction evolution from the matrix to the top of the melt pool. The location-specific phase-fraction variation is clearly demonstrated. It should be noted that although this measurement was originally designed to identify the phase fractions along the vertical centerline in the melt pool cross-section, it is difficult to position the X-ray beam at the exact centerline. Therefore, the measured line profile locations could be shifted slightly (5 μm to 10 μm) from the centerline. In this measurement, as indicated from Fig. 5(c), the position #15 is the top of the melt pool surface, where the BCC β phase signal is last observed in the XRD pattern and considered as the melt pool top surface. The peak intensities in position #16 and further positions were several orders of magnitude lower than #15. Hence, these positions are no longer considered as part of the melt pool. From Fig. 5(d), the starting plateau from the melt pool (from positions 15) shows a near-constant small amount of HCP α phase, representing the melt pool region. Proceeding vertically, a transition region appears, representing the heat affected zone observed in Fig. 3, where the melt pool boundary could be potentially at positions 8 or 9. Based on the 5 μm step size in HR-XRD measurement, this

Table 2
Parameters for CFD and CALPHAD simulations.

CFD Parameters			
Parameter	Value	Unit	Source
Thermal conductivity of solid	1.4984 + 0.01510T	$W•m^{-1}•K^{-1}$	Ti-64 [23]
Thermal conductivity of liquid	5.5613 + 0.01782T	$W•m^{-1}•K^{-1}$	Ti-64 [23]
Specific heat capacity for solid	767.0100	$J•kg^{-1}•K^{-1}$	Database*
Specific heat capacity for liquid	972.0050	$J•g^{-1}•K^{-1}$	Database*
Density	4.45×10^3	$kg•m^{-3}$	Weighted average**
Laser Speed	varies	mm/s	Experimental Setup Parameters
Laser Power	100	W	
Laser spot radius	30	μm	
Latent heat of fusion	Temperature-dependent	$J•kg^{-1}•K^{-1}$	Database*
Dynamic viscosity	Temperature-dependent	Pa•s	Weighted average****
Surface tension gradient	Temperature-dependent	$N•m^{-1}•K^{-1}$	Weighted average***
Thermal expansion coefficient	0.000015424	K^{-1}	Weighted average**
Liquidus Temperature	1899.4400	K	Database*
Solidus Temperature	1788.7300	K	Database*
Coefficient of convective heat transfer	0.05	$W•m^{-2}•K^{-1}$	Calibrated
Laser Absorptivity	0.50	–	Calibrated
Emissivity	0.40	–	Calibrated
CALPHAD Parameters			
Molar volume	Composition-dependent	m^3/mol	Database*
Interfacial energy*****	Temperature/composition-dependent	J/m^2	Database*
Needle morphology aspect ratio	3	N/A	Experimental observation

* Database: customized Ti-Al-Fe database in this work.
** Pure element data from source [24].
*** Pure element data from source [25].
**** Pure element data from source [26].
***** Calculated using extended Becker's model, temperature and composition dependent [20].

line profile has a melt pool depth of 30 μm to 35 μm. When validating, the CALPHAD simulations with closest melt pool depths were used to compare with the HR-XRD measurements.

3.2. Model development

3.2.1. CFD simulation setup and assumptions

To predict the melt-pool geometry and cooling rates during the single laser track, a 3-dimensional transient thermal-fluid model based upon CFD is used in the study [12]. This thermal-fluid model considers liquid flow within the melt-pool driven by the Benard-Marangoni effect to provide physically sound temperature fields. The CFD simulation utilizes the same build parameters in the single laser track experiments, including laser speed, laser power and the radius of the laser beam. Additionally, the material properties of this Ti-Al-Fe in the experiments are calculated by the CALPHAD method. These parameters are listed in Table 2. With this information, and assuming an approximate primary dendrite arm spacing of 1.6 μm, the thermal-fluid model predicts the location-specific temperature profiles within the part.

In addition to the single laser track, a 4-track simulation is also conducted. As observed in the single laser tracks, the heat affected zone from multiple thermal cycles is expected to significantly impact the layer-by-layer AM builds. This simulation is designed to emulate this condition and predict the impact of heat affected zone in actual AM build environment. There are in total 4 parallel laser tracks deposited with the same laser scan direction and 50 μm hatch spacing.

3.2.2. CALPHAD simulation assumptions and starting conditions

The as-cast bare plate was characterized by HE-XRD to determine the starting α and β phase fractions. The starting α phase volume fraction was defined as 75.7% in TC-PRISMA based on experimental measurements. The starting α phase size distribution is another important input into the TC-PRISMA simulation, from the Lifshitz-Slyozov-Wagner (LSW) model and based on metallurgical observation [8], a mean size of 10 nm was assumed. Since the HR-XRD measurement was conducted at the location where the melt pool depth is 30 μm to 35 μm, the CALPHAD validation simulations were conducted at two line profiles with closest simulated melt pool depths, 30 μm and 37.5 μm respectively.

Table 3
Calculated β transus and T_0 for Ti-6Al-4 V and Ti-6Al-5Fe.

	T_0 (K)	β transus (K)
Ti-6Al-4V	1102	1193
Ti-6Al-5Fe	457	1126

It should be noted that in AM process for commercial titanium alloy, such as Ti-64, it is common to observe the phase transformation of β to martensitic α' instead of α phase, which is also a possibility for this Ti-Al-Fe alloy in the melt pool. However, as for the rapid solidification region in the melt pool, it can be observed from the BSD that there hardly exists α or α' phase (by Z-contrast and morphology). On the other hand, HR-XRD showed small amount of HCP structure, which could be either α or α' phase. However, if the diffusionless nature of β-to-α' transformation is considered and potential nucleation sites for α' exist, the resulting α' phase fraction should be enormous and with clear acicular morphology as shown in SLM Ti-64 [22]. While in this investigation, the current experimental evidence does not suggest that the HCP structure in the melt pool region is α' but diffusional α phase.

In addition, fundamental consideration of Ti metallurgy provides additional confidence for the exclusion of α'. In Ti-Al-Fe system, the diffusion kinetics is much faster than in most commercial Ti alloy system (e.g. compared with V in β phase). The faster diffusion makes diffusional transformation possible even under typical AM-range cooling rate, hence suppressing the martensitic transformation. We calculated the temperature differences between β transus and $\mathbf{T_0}$. They are listed in Table 3. Evidently, due to the small gap between $\mathbf{T_0}$ and β transus in Ti-6Al-4 V, it will be significantly more difficult to suppress the martensitic transformation than in Ti-6Al-5Fe, where the gap is approximately 7 times greater. Therefore, it is likely that the martensitic transformation in this new Ti-Al-Fe alloy is mostly suppressed.

Table 4
Metallurgically-measured and simulated melt pool centerline depth.

Laser Speed (mm/s)	Melt pool centerline depth (μm)	
	Experiment	Simulation
400	163.925	161.250
700	76.077	73.6250
1000	49.773	46.250

3.2.3. Parameters for CFD and CALPHAD simulations

For this specific Ti-Al-Fe α-β titanium alloy, the materials and simulation parameters and their sources are listed in Table 2. Sources of these parameters are from the customized thermodynamic and kinetic database developed in this work, weighted averages of pure element data, approximations based on a current α-β commercial titanium alloy, and model calibration. The weighted average from pure elements is applied as $\sum_i x_i P_i$, on certain properties that do not have widely accepted models, in which $x_i$and $P_i$are the mole fraction and the material property of the pure element, respectively. Parameters that neither follow weighted averages nor have models are approximated from existing commercial α-β titanium alloys, which is Ti-64 in this work. It should be noted that the value of the absorptivity, coefficient of convective heat transfer, and emissivity are calibrated based on the radiant temperature from the top surfaces. Although the temperatures measured in the experiments differ from those predicted in the simulations due to measurement calibrations, the phase transition from liquid to solid and the associated lengths of the melt-pools are in qualitative agreement.

3.3. Modeling results and discussion

3.3.1. Temperature evolution below melt pool surface

Based on CFD simulation result for each location, the temperature evolutions below the bare alloy plate were plotted in Fig. 6 at selected time steps. The solidus contours expand first and shrink afterwards, indicating the laser approaching, melting, laser leaving, and solidification. For each location, if its temperature ever reached above alloy solidus, then it was defined as part of the melt pool, or otherwise, as part of the unmelted bare alloy plate. It can be seen from Table 4 that the simulated and experimental measured melt pool depths agreed well.

On the other hand, in Fig. 6, the β transus contours do not behave the same as the solidus contours. The β transus contours continue to expand after the melt and solidification complete due to the intensive heat and the low thermal conductivity of titanium alloys. This simulation result correlates with the experimental observation of the heat affected zones and further quantified by CALPHAD phase transformation simulation.

To quantitatively simulate heat affected zones based on the CALPHAD simulations, the location-specific temperature profiles from CFD simulation were extracted. Fig. 7 shows the series of profiles along the melt pool centerline at all 3 laser speeds, illustrating the spatial evolution of temperature profiles. As shown, all temperature profiles rapidly reach peak temperatures and then exponentially decrease to room temperature. The details of the CFD simulation are not the focus in this paper and will be described in-depth in a separate paper.

3.3.2. CALPHAD validation simulations in the 700 mm/s single laser track

Fig. 8(a) and (b) showed the comparisons between HR-XRD measured α phase fraction and CALPHAD simulations at two possible measured line profiles with melt pool depths of 30 μm and 37.5 μm, respectively. The calculated heat affected regions and melt pools agreed well with both microscopy observations and HR-XRD measurements. There were some discrepancies in the α phase fraction values in the heat affected zones, which could be attributed to two possible causes: CALPHAD simulation assumptions and HR-XRD measurement limitation. An important assumption made in the CALPHAD simulation is the starting α phase size distribution. The size distribution will affect the growth and dissolution driving forces of certain size clusters. As for experimental measurements, each HR-XRD step acquires signal from the entire 1 mm thickness throughout the specimen in a 10 μm x 5 μm area. Therefore, any inhomogeneities across the 1 mm thickness could have resulted from laser fluctuations or localized metal plate surface reflections. In such cases, the HR-XRD measurements represent the sum of multiple cross-sections throughout the specimen and will depart from the idealized conditions from CALPHAD simulation.

3.3.3. CALPHAD simulations in all single laser tracks

Based on experimental validation above, Fig. 9 shows the CALPHAD simulated location-specific final α phase volume fraction maps for all 3 laser speeds and is correlated with cross-section microscopy. The simulations at all 3 laser speeds are in good agreement with melt pool morphologies. The heat affected zones predicted by simulations at 700 mm/s and 1000 mm/s speeds also qualitatively agree with microscopical observation. On the other hand, heat affected zone predicted in the 400 mm/s simulation is larger than what is observed. This discrepancy, similar to CFD results, could be due to the assumption in CFD simulation that the heat transfer is isotropic, while experimental observation shows that since the heat affected zone width is obviously larger close to the melt pool surface, especially in a keyholing observed at the 400 mm/s laser speed, implying heat transfer was slower vertically than horizontally.

3.3.4. Melt pool geometry and phase transformation in the multiple overlapping laser tracks

Fig. 10(a) shows the maximal reached temperature contour in the four-track simulation. It is shown that the melt pools increased slightly in size due to the contributions of residual heat from the previous melt pools. Fig. 10(b) shows several temperature profiles at different melt pool positions, which clearly illustrate the interaction among laser tracks. Similar to the result from single laser track, the phase transformation is closely associated with the temperature profile, but the final phase fraction is determined by the sum of all thermal cycles instead of from a single profile. The effect is observed in the melt pool final α phase fraction evolution maps in Fig. 10(c). The different time steps corresponded to the initial condition (0 s), the end of 1st thermal cycle (0.015 s), the end of 2nd thermal cycle (0.03 s), the end of 3rd thermal cycle (0.045 s), and the end of the experiment (0.06252 s), respectively. It clearly shows that as the continuation of multiple laser tracks, the phase transformation of the 1st laser track is strongly affected by the neighboring tracks, proving the significance of the heat affected zone effect in determining as-fabricated microstructures and properties for this specific titanium alloy.

3.3.5. Impact of heat affected zone in actual AM build

First observed in welding, the heat-affected zone occurs at high-temperatures when an un-melted regime forms as a result of intensive heat from neighboring fusion regime [27]. The region may then undergo a phase transformation during cooling and alter the microstructure and properties associated with the region. In titanium additive manufacturing, a heat-affected zone was also observed, especially for a relatively large energy input and melt pool size [3,28,29], but it is not observed under small energy input [30]. This phenomenon is important in a real AM environment. The AM component is constructed layer-by-layer, and each layer will undergo multiple thermal cycles from melting to heat treatment due to residual heat from adjacent layers. Therefore, the as-fabricated microstructure will be determined by the combined effect of all thermal cycles instead of just the initial solidification in the melt pool. This is especially true for kinetically susceptible materials, such as the Ti-Al-Fe alloy in this investigation. This effect could be detrimental in creating an inhomogeneous microstructure that promotes premature failure. Likewise, it may be possible to tailor the heat-affected regions

to create location-specific microstructures that improve the part performance.

As illustrated in Fig. 10(c), the heat affected zone phenomenon has a significant impact on the melt pool microstructure, which is directly correlated to as-fabricated properties. As shown, with the same laser parameters, a layer-by-layer scanning could result in severe inhomogeneity in as-fabricated microstructure, and thus cause unwanted microstructural features and properties. This result shows that to avoid this issue, the laser and build setup need to be adjusted accordingly in power/speed to control the effect of heat affected zone. At the same time, as discussed above, it also indicates that the microstructure, α phase fraction in this case, can be engineered to acquire location-specific properties for certain applications.

4. Conclusion

This paper established a combined CFD/CALPHAD computational framework aimed at AM phase transformation prediction in this Ti-Al-Fe alloy. This work shows that with well-established thermodynamic and kinetics databases and sufficient experimental details for the macroscale simulation, the phase transformation in AM environment can be accurately predicted, even for new alloys with scarce experimental information, such as the Ti-Al-Fe alloy in this work. As the experimental and modeling results indicated, the Ti-Al-Fe alloy system is a strong candidate for AM process and its as-fabricated microstructure and properties can be engineered with the modeling framework in this work. For the alloy in this work, the heat affected zone is accurately captured and its potential location-specific effect in actual AM build is also predicted. The modeling framework combined with single laser track validation experiments can be applied to rapidly predict and evaluate the performance of new titanium alloy systems in AM environment, and thus significantly accelerate new AM titanium alloy design. In addition, with the appropriate thermodynamic and kinetic databases and selected single laser track experiments, this CFD-CALPHAD can be used to evaluate prototype alloys for a wide-range of alloy systems for AM processing.

Declaration of Competing Interest

The authors declare that they have no known competing financial interests or personal relationships that could have appeared to influence the work reported in this paper.

Acknowledgement

Use of the Advanced Photon Source, an Office of Science User Facility operated for the U.S. Department of Energy (DOE) Office of Science by Argonne National Laboratory, was supported by the U.S. DOE under Contract No. DE-AC02-06CH11357. Fan Zhang would like to thank Dr. Uta Ruett of the Advanced Photon Source for her help with setting up microfocus X-ray diffraction.

Supplementary materials

Supplementary material associated with this article can be found, in the online version, at doi:10.1016/j.mtla.2020.100934.

References

[1] G. Lütjering, J.C. Williams, Titanium, 2nd Ed., Springer Berlin Heidelberg, 2007.
[2] S.L. Semiatin, An Overview of the thermomechanical processing of α/β titanium alloys: current status and future research opportunities, Metall. Mater. Trans. A (2020).
[3] S. Liu, Y.C. Shin, Additive manufacturing of Ti6Al4V alloy: a review, Mater Des 164 (2019) 107552.
[4] A.B. Badiru, V.V. Valencia, D. Liu, Additive Manufacturing Handbook: Product Development For the Defense Industry, CRC Press, 2017.
[5] A. Mitchell, Melting, casting, and forging problems in titanium alloys, JOM 49 (6) (1997) 40–42.
[6] A. Mitchell, A. Kawakami, S.L. Cockcroft, Beta fleck and segregation in titanium alloy ingots, High Temp. Mater. Processes (London) (2006) 337.
[7] Z. Liang, J. Miao, R. Shi, J.C. Williams, A.A. Luo, CALPHAD modeling and experimental assessment of Ti-Al-Mn ternary system, Calphad 63 (2018) 126–133.
[8] Z. Liang, J. Miao, T. Brown, A.K. Sachdev, J.C. Williams, A.A. Luo, A low-cost and high-strength Ti-Al-Fe-based cast titanium alloy for structural applications, Scr. Mater. 157 (2018) 124–128.
[9] R.E. Ricker, J.C. Heigel, B.M. Lane, I. Zhirnov, L.E. Levine, Topographic measurement of individual laser tracks in alloy 625 bare plates, Integr. Mater. Manuf. Innov. 8 (4) (2019) 521–536.
[10] B. Lane, J. Heigel, R. Ricker, I. Zhirnov, V. Khromschenko, J. Weaver, T. Phan, M. Stoudt, S. Mekhontsev, L. Levine, Measurements of melt pool geometry and cooling rates of individual laser traces on IN625 bare plates, Integr. Mater. Manuf. Innov. 9 (1) (2020) 16–30.
[11] G. Lindwall, C.E. Campbell, E.A. Lass, F. Zhang, M.R. Stoudt, A.J. Allen, L.E. Levine, Simulation of TTT curves for additively manufactured inconel 625, Metall. Mater. Trans. A 50 (1) (2019) 457–467.
[12] Z. Gan, Y. Lian, S.E. Lin, K.K. Jones, W.K. Liu, G.J. Wagner, Benchmark study of thermal behavior, surface topography, and dendritic microstructure in selective laser melting of inconel 625, Integr. Mater. Manuf. Innov. 8 (2) (2019) 178–193.
[13] J.F. Murdock, T.S. Lundy, E.E. Stansbury, Diffusion of Ti44 and V48 in titanium, Acta Metall. 12 (9) (1964) 1033–1039.
[14] R. Borg, C. E. Birchenall, Self-diffusion in alpha iron, AIME 218 (6) (1960) 980–984.
[15] I.A. Akimova, V.M. Mironov, A.V. Pokoyev, The diffusion of aluminium in iron, Fiz. Met. Metalloved 56 (6) (1983) 1225–1227.
[16] H. Araki, T. Yamane, Y. Minamino, S. Saji, Y. Hana, S.B. Jung, Anomalous diffusion of aluminum in β-titanium, Metall. Mater. Trans. A 25 (4) (1994) 874–876.
[17] H. Wu, T. Mayeshiba, D. Morgan, High-throughput ab-initio dilute solute diffusion database, Sci Data 3 (1) (2016) 160054.
[18] G.B. Gibbs, D. Graham, D.H. Tomlin, Diffusion in titanium and titanium—niobium alloys, Philosoph. Magazine 8 (92) (1963) 1269–1282.
[19] R. Wagner, R. Kampmann, P.W. Voorhees, Homogeneous second-phase precipitation, in: G. Kostorz (Ed.), Phase Transformations in Materials, Wiley-VCH Verlag GmbH, Weinheim, Germany, 2001, pp. 309–407.
[20] ThermoCalc, The Precipitation module (TC-PRISMA) user guide 2020a. https://www.thermocalc.com/support/documentation/, (accessed June 30 2019,).
[21] W.E. King, H.D. Barth, V.M. Castillo, G.F. Gallegos, J.W. Gibbs, D.E. Hahn, C. Kamath, A.M. Rubenchik, Observation of keyhole-mode laser melting in laser powder-bed fusion additive manufacturing, J. Mater. Process. Technol. 214 (12) (2014) 2915–2925.
[22] J. Yang, H. Yu, J. Yin, M. Gao, Z. Wang, X. Zeng, Formation and control of martensite in Ti-6Al-4V alloy produced by selective laser melting, Mater. Des. 108 (2016) 308–318.
[23] M. Boivineau, C. Cagran, D. Doytier, V. Eyraud, M.-.H. Nadal, B. Wilthan, G. Pottlacher, Thermophysical properties of solid and liquid Ti-6Al-4V (TA6V) alloy, Int. J. Thermophys. 27 (2) (2006) 507–529.
[24] Coefficients of linear thermal expansion. https://www.engineeringtoolbox.com/linear-expansion-coefficients-d_95.html, 2003 (accessed May 21st 2020).
[25] A.I.H. Committee, ASM Handbook, ASM International, Materials Park, OH, 2008.
[26] L. Battezzati, A.L. Greer, The viscosity of liquid metals and alloys, Acta Metall. 37 (7) (1989) 1791–1802.
[27] B. Nesbitt, Handbook of valves and actuators: valves manual international, Elsevier Science, 2011.
[28] T. Wang, Y.Y. Zhu, S.Q. Zhang, H.B. Tang, H.M. Wang, Grain morphology evolution behavior of titanium alloy components during laser melting deposition additive manufacturing, J. Alloys Compd. 632 (2015) 505–513.
[29] Y.-Y. Zhu, H.-B. Tang, Z. Li, C. Xu, B. He, Solidification behavior and grain morphology of laser additive manufacturing titanium alloys, J. Alloys Compd. 777 (2019) 712–716.
[30] H. Gong, H. Gu, K. Zeng, J.J.S. Dilip, D. Pal, B. Stucker, D.E. Christiansen, J.J. Lewandowski, Melt pool characterization for selective laser melting of Ti-6Al-4V pre-alloyed powder, in: D.L. Bourell (Ed.), Solid Freeform Fabrication Proceedings, University of Texas, Austin, TX, 2014, pp. 256–267.